Processing and Application of Ceramics 12 [2] (2018) 100–110
https://doi.org/10.2298/PAC1802100D

Structural, morphological, magnetic and electrical properties of Ni-doped ZnO nanoparticles synthesized by co-precipitation method

Madhava P. Dasari[1,*], Umadevi Godavarti[1,2], Vishwanath Mote[3]

[1]*Department of Physics, GIT, Gitam University, Visakhapatnam - 530 045, A. P., India*
[2]*CMR Technical Campus, Medchel, Hyderabad - 501 401, Telangana, India*
[3]*Department of Physics, Dayanand Science College, Latur - 413 512, Maharashtra, India*

Received 14 September 2017; Received in revised form 4 January 2018; Received in revised form 24 March 2018; Accepted 11 April 2018

Abstract

Weak ferromagnetic behaviour was obtained in a systematic way at room temperature by doping of ZnO with nickel ($Zn_{1-x}Ni_xO$, where x = 0.00, 0.05, 0.15 and 0.20). The obtained results were correlated with conductivity and impedance studies. Diamagnetic to ferromagnetic change was observed with increased concentration of nickel. X-ray diffraction analysis confirmed wurtzite ZnO structure of prepared nanopowders while microstrain was increased with nickel concentration. Incorporation of nickel in ZnO structure was confirmed using EDAX analysis, while FTIR spectroscopy provided further information on functional groups. Transmission electron microscopy images showed that the particle sizes are in the range of 12–20 nm, and scanning electron microscopy analyses that grain size decreases with increase in nickel concentration. Photo luminescence studies confirmed the presence of V_O and Zn_i defects in the prepared samples. It was concluded that the defect induced strain, grain boundaries and lower particle sizes are the reasons for weak ferromagnetic behaviour of the investigated samples.

Keywords: *co-precipitation, ZnO, magnetic properties, conductivity, impedance studies*

I. Introduction

ZnO, n-type host semiconductor, is an interesting material due to its wide band gap (E_g = 3.37 eV), large exciton binding energy (~60 meV), an absence of toxicity and easiness of synthesis in stable hexagonal wurtzite structure. Doped ZnO semiconducting materials with transition metals (TM) can combine both charge and spin degrees of freedom in a single substance as possible building blocks for spintronics devices. Further, TM-doping in ZnO improves optical, electrical and mechanical properties due to quantum confinement effects.

In view of the spintronic applications [1,2], the foremost parameter that characterizes ferromagnetic materials is the degree of spin polarization of band carriers. II-VI TM-doped semiconductors have shown lower defect concentrations and ferromagnetism mainly due to the intrinsic defects or impurity phases [3,4]. Some of the widespread applications include LEDs [5–7], UV-absorbers [8], solar cells [9–11] and spintronics. Due to its unusual conducting properties, ZnO has also been deliberated as a transparent conducting and piezoelectric material for the use in electrodes and sensors [12–14].

Transition metals (Sc, Ti, V, Cr, Mn, Fe, Co, Ni, and Cu) that have partially filled *d*-states or rare earth metals which have partially filled *f*-states (e.g. Eu, Gd, Er) induce ferromagnetism due to the presence of magnetic atoms in diluted magnetic semiconductors (DMS). Ferromagnetism arises due to the exchange mechanism of the doped cations into the tetrahedral and octahedral sites of wurtzite structure [15–18].

The addition of nickel with 0.6 μ_B to ZnO could lead to weak ferromagnetic behaviour up to 350 K, a suitability criterion for diluted magnetic semiconductors (DMS) materials [19,20]. Haq *et al.* [21] and Schwartz *et al.* [22] stated that by Ni-doping of ZnO ($Zn_{1-x}Ni_xO$) nanoparticles AFM (antiferromagnetic) coupling and ferromagnetic interaction are also possible. These substituting ions replacing zinc also acts as electron dopants due to their trivalent valence. The correlation between

*Corresponding author: tel: +91 9348811777,
e-mail: *madhavaprasaddasari@gmail.com*

the conductivity and magnetic properties can be further studied and understood on the basis of availability of electrons in the bands which are localized in the 3*d* orbital.

In this paper, ZnO was doped with nickel and small improvement in magnetic and conductivity properties of ZnO, desired for DMS applications, could be expected. The proof of Ni-doping could be evidenced by structural or morphological variation which can be observed through X-ray diffraction. The strive of these studies is to understand the vacancy induced magnetism and exchange coupling among *p-d* resulting variations observed based on band carriers and localized spins.

II. Experimental procedure

All precursor materials are of high purity analytical grade. Zinc acetate dihydrate ($Zn(CH_3COO)_2 \cdot 2\,H_2O$), nickel acetate tetrahydrate ($Ni(OCOCH_3)_2 \cdot 4\,H_2O$) and sodium hydroxide (NaOH), were purchased from Sigma-Aldrich and ethanol and methanol (99.998%) were used as the solvents without further purification.

The pure ZnO nanoparticles (NPs) were prepared by separately dissolving stoichiometric amounts of zinc acetate and NaOH in 50 ml methanol. The obtained NaOH solution was added dropwise to the prepared zinc acetate in methanol and then stirred continuously with heating at 325 K for 2 h. The precipitate was separated from the solution by filtration, washed several times with distilled water and ethanol then dried in air at 400 K to obtain ZnO nanocrystals. The obtained samples were annealed at 673 K for 8 hours.

For the synthesis of the Ni-doped samples ($Zn_{1-x}Ni_xO$ where x = 0.05, 0.15, 0.20) the same procedure was used. Zinc acetate dihydrate and nickel acetate tetrahydrate were dissolved in methanol (100 ml) and NaOH in methanol (100 ml) was prepared separately. The obtained NaOH solution was added to the precursor solution during constant magnetic stirring while heating at 325 K for 2 h. The obtained precipitate was separated from the solution by filtration, washed several times with distilled water and ethanol then dried in air at 400 K. The obtained samples were annealed in air for 8 h at 673 K.

The samples were characterized by using XPERT-PRO (PW: 3710) X-ray diffractometer (XRD) with Cu Kα radiation source of wavelength 1.54056 Å, recorded at room temperature over the 2θ range of 20° to 80° to understand the crystallinity and phase orientation of the pure and doped ZnO nanoparticles. The surface morphology, size distribution and the composition of the elements of the prepared samples were determined with scanning electron microscope (SEM, JSM 6100) using image analyser. Transmission electron microscope (TEM) images were captured by using Hitachi, H-7500 microscope. Magnetization measurements of the undoped and Ni-doped ZnO nanostructures were obtained by using vibrating sample magnetometer (VSM, Princeton applied research model EG&G-4500). The optical absorption/ transmission spectra of ZnO and Ni-substituted ZnO nanoparticles were recorded using a UV-NIR-3600 spectrophotometer. The photoluminescence (PL) spectrum of the undoped and Ni-doped ZnO nanoparticles have been measured using a Perkin Elmer 45 fluorescence spectrometer.

III. Results and discussion

3.1. Structural analysis - XRD

X-ray powder diffraction (XRD) was studied to determine the structural parameters of the doped ZnO nanoparticles. XRD diffraction patterns of ($Zn_{1-x}Ni_xO$ where x = 0.05, 0.15, 0.20) NPs are presented in Fig. 1. Peak positions of Ni-doped ZnO correspond to the standard Bragg positions of hexagonal wurtzite ZnO. The XRD patterns show only peaks of the pure hexagonal wurtzite ZnO phase, which is in good agreement with the JCPDS data (card number 89-1397). XRD analysis confirmed also the presence of secondary phase of NiO in the sample with 20 at.% of Ni. This may come from the attainment of saturated state of doping level [23,24].

Broad nature of diffraction peaks due to the microstrain also indicates the nanosize nature of the prepared pure and Ni-doped ZnO NPs. Full width half maxima (FWHM) from XRD analysis decreases with decrease in Ni^{2+} concentration, indicating crystallite growth [25]. The average crystallite size estimated using Debye-Scherrer's equation for the pure ZnO nanoparticles is calculated as 57 nm and found to decrease with the Ni doping concentration as shown in Table 1.

The strain can be calculated by the formula:

$$\varepsilon = \frac{\beta}{4 \cdot \tan\theta} \tag{1}$$

The strain increases with increase of nickel concentration was also observed (Table 1).

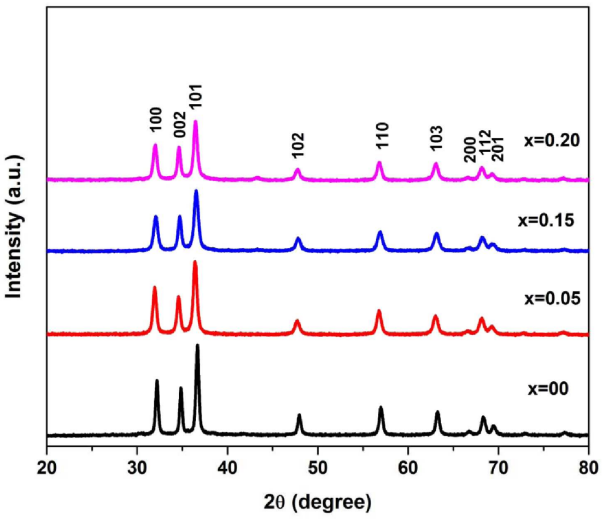

Figure 1. XRD patterns of Ni-doped $Zn_{1-x}Ni_xO$ samples

Table 1. Lattice parameters of undoped and Ni-doped samples

Ni concentration [at.%]	a [Å]	c [Å]	L [Å]	V [Å^3]	D [nm]	Microstrain ε
0	3.2088	5.1477	1.9536	45.9003	57	0.002444
5	3.1607	5.0607	1.9232	43.7819	52	0.002759
15	3.1562	5.0606	1.9213	43.6565	43	0.002953
20	3.1499	5.0601	1.9186	43.4781	43	0.003414

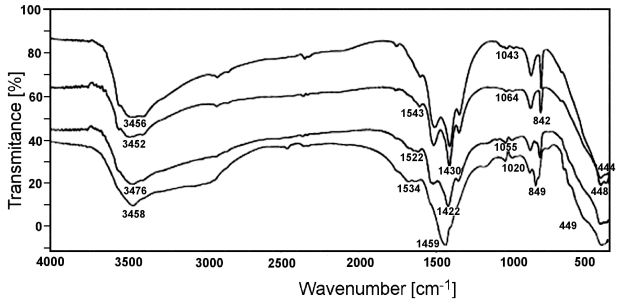

Figure 2. FTIR spectra of $Zn_{1-x}Ni_xO$ samples

The lattice parameters a and c for the pure hexagonal wurtzite structured and Ni-doped ZnO nanoparticles are calculated from the equation:

$$\sin^2\theta = \frac{\lambda^2}{4a^2}\left(\frac{4}{3}\left(h^2 + hk + k^2\right) + \frac{a^2 \cdot l^2}{c^2}\right) \qquad (2)$$

The changes in a and c lattice parameters are observed due to the Ni-doping. The decrease in lattice parameters can be attributed to the replacement of larger Zn^{2+} (0.60 Å) ions with smaller Ni^{2+} ions (0.55 Å). These results are supported well with literature data [25].

The volume of unit cell can be determined by the following formula:

$$V = 0.8666 \cdot a^2 \cdot c \qquad (3)$$

With the increase in the concentration of nickel in ZnO, the volume of the unit cell decreases, suggesting the incorporation in the inner lattice of Zn ions. This could be correlated from the decrease of crystallite size or decreasing lattice parameters. This further affects the bond length, which also reduces due to the increased micro strain as shown in Table 1.

The structural changes attained from the diffraction peaks indicate that Ni^{2+} is successfully incorporated into ZnO lattice, which further means no changes in the crystal lattice by the Ni-doping [26].

3.2. Structural analysis - FTIR

The formation of wurtzite structure of Ni-ZnO was further supported by FTIR measurements. FTIR spectra for the pure and Ni-doped ZnO nanoparticles were recorded in the range of 4000–400 cm^{-1} and are shown in Fig. 2 with characteristic bands given in Table 2. The absorption bands at 451 cm^{-1} are attributed to the Zn–O hexagonal vibration modes. The absorption peak that appears at 3440 cm^{-1} is attributed to O–H stretching vibrations of H_2O. The peak around 1640 cm^{-1} is due to the H–O–H bending vibration, which is assigned to a small amount of H_2O in ZnO NPs. The absorption peak observed at 2917 cm^{-1} is due to the existence of CO_2 molecules in the air. The medium to a weak band at 840 cm^{-1} is assigned to the metal–oxygen vibration frequency due to the changes in the microstructural features by the addition of Ni into the ZnO lattice. It is observed from IR spectra for the Ni-doped samples that the peak found at 3460 cm^{-1} is assigned to the –OH mode in the H_2O molecules. The presence of these bands in the synthesized nanoparticles may be due to the adsorption of atmospheric water content. The bands around 1040 cm^{-1} are shoulders with asymmetric stretching of resonance interaction between vibration modes of oxide ions in the nanocrystals. Zn–O stretching is exhibited at different wave numbers tabulated in Table 2 with absorption values well supported by the literature data [27].

3.3. Structural analysis - SEM

The surface morphology of the prepared ZnO NPs reveals spherical structure, as shown in Fig. 3. The morphology of the nickel doped ZnO samples shows a random hexagonal and spherical structure with smaller grain size compared to the pure ZnO. Patricles are non-homogeneous and they appear to be broadly agglomerated. The particles tend to agglomerate with one another due to the increase in surface to volume ratio which results an increase in attractive force, attributed to nickel incorporation in ZnO lattice. The decrease

Table 2. FTIR vibrational modes of $Zn_{1-x}Ni_xO$

Functional group / chemical species	Ni concentration, [at.%]			
	0	5	15	20
O–H stretching	3458	3476	3452	3456
H–O–H bending vibration	1694	1522	1543	-
Acetate group stretching	1459	1422	1430	1427
O–H asymmetric stretching	1020	1055	1064	1063
Weak vibrations of ZnO	849	839	842	842
Zn–O stretching	434	443	448	444

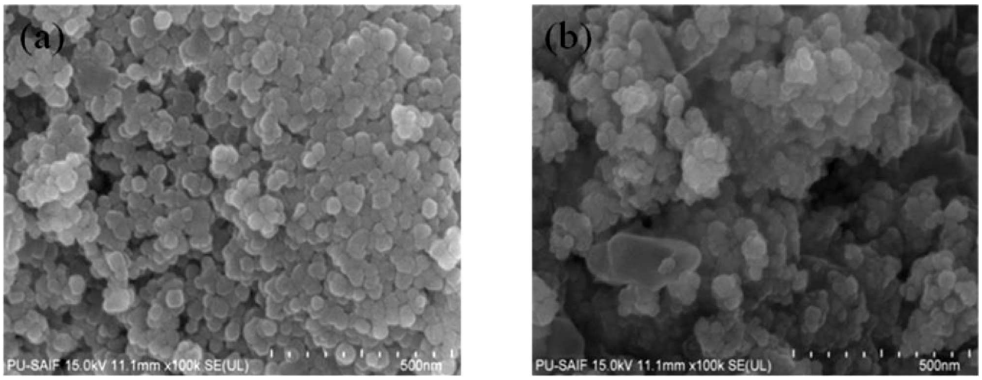

Figure 3. SEM images of: a) undoped and b) doped ZnO with 20 at.% Ni

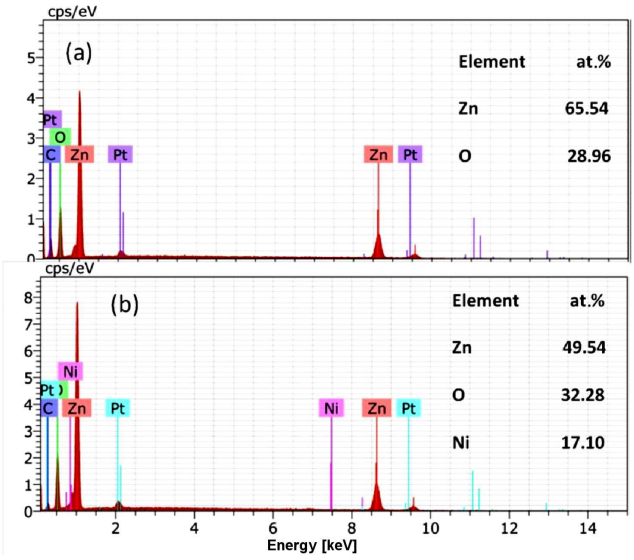

Figure 4. EDX spectra of: a) undoped and b) doped ZnO with 20 at.% Ni

in grain size with increasing doping concentration is observed and the same behaviour is reported by Vijayaprasath [28,29].

3.4. Structural analysis - EDX

Compositional analysis, done by energy-dispersive X-ray spectroscopy (EDX), is shown in Fig. 4 in the presence of platinum in the carbon/metal hybrid microtubes [30]. The appearance of C peak in the spectrum is attributed to the emission of carbon tape used during the EDX measurement. The observation of low intensity peak for nickel doped ZnO in Fig. 4b, shows the proper incorporation of nickel in the structure.

3.5. Structural analysis - TEM

TEM micrographs of the $Zn_{1-x}Ni_xO$ samples (Fig. 5) indicate on the formation of spherical nanosized particles with well-confined but agglomerated structure. The average size of the pure ZnO particles estimated by TEM is around 29 nm. However, the average crystallite size calculated from XRD by Debye Scherrer equation is 57 nm and this variation in size from XRD and TEM could be caused by the presence of strain. Particle sizes calculated using TEM for the Ni-doped NPs for x = 0.05, 0.15, and 0.20 are 21, 18 and 12 nm, respectively. The decreasing trend is correlated with results of X-ray diffraction.

3.6. Structural analysis - Photoluminescence

The presence of defects in Ni-ZnO nanoparticles was investigated by photoluminescence measurements (Fig. 6, Table 3). In general, defects present in ZnO based nanostructures are oxygen vacancies, Zn vacancies, Zn interstitials and adsorbed molecules [31] and can be analysed according to the several transitions located between the valence and conduction band. To understand the origin of the emission peaks of the spectral region 350–800 nm, Gaussian fitting method of the broad visible emission was adopted to study the individual effects on the properties of ZnO nanostructures.

The UV emission at approximately 380 nm corresponds to the exciton recombination due to the near-band emission (NBE) of ZnO. The emission peak at 410–490 nm may be due to the electron transition from Zn interstitial energy level to the valence band (440 nm), or may be attributed due to the transition between oxygen vacancy and interstitial oxygen (488.5, 477 nm). V_O related defects and V_{Zn} contribute to the broad band

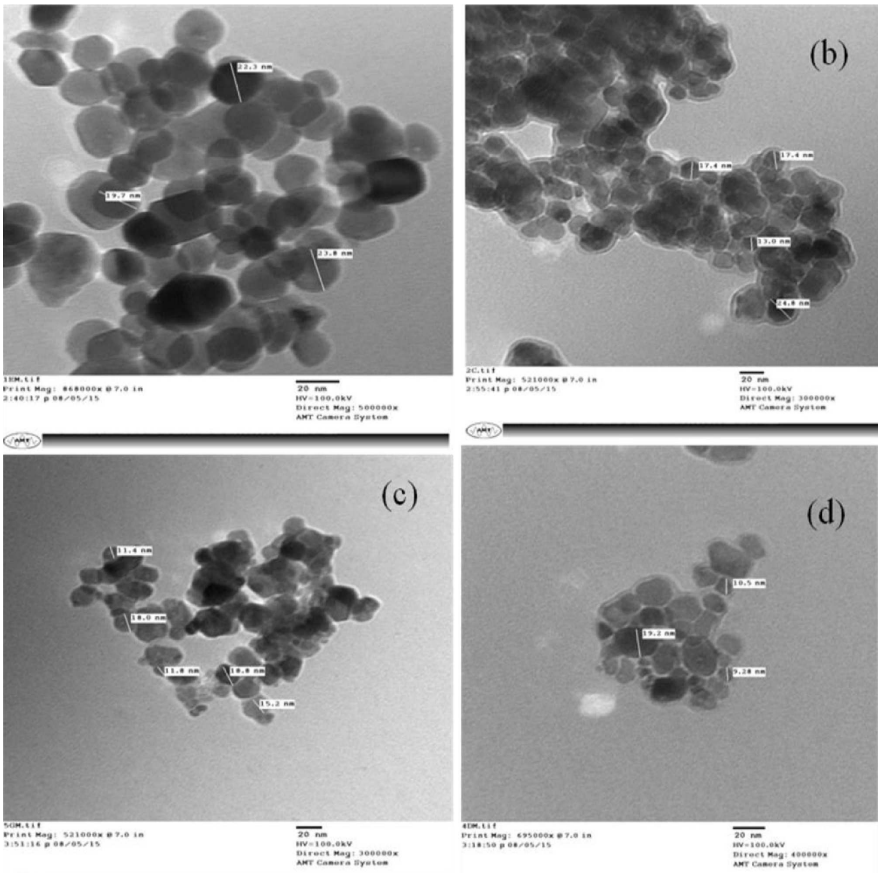

Figure 5. TEM images for pure ZnO (a) and Ni-doped $Zn_{1-x}Ni_xO$ nanoparticles with: b) 5, c) 15 and d) 20 at.% Ni

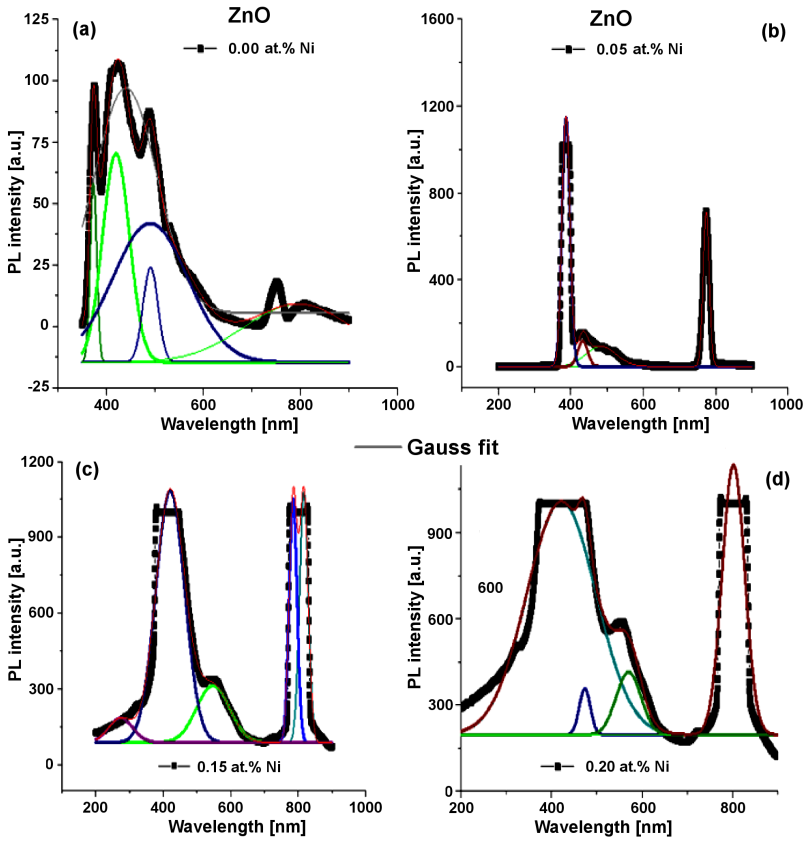

Figure 6. PL spectra of pure ZnO (a) and Ni-doped $Zn_{1-x}Ni_xO$ nanoparticles with: b) 5, c) 15 and d) 20 at.% Ni

Table 3. Photoluminescence emission peaks for undoped and doped ZnO nanoparticles

Ni concentraton [at.%]	NBE [nm]	Violet emission [nm]	Blue emission [nm]	Green emission [nm]	Orange-red emission [nm]
0	374, 366.5	424	441, 488.5	525	733, 754
5	383.5	-	437	500.5	775
15	380	419.5	444.5	553	784, 817.5
20	386.5	421.5	477, 469.5, 476	554.5, 563, 571	772, 829.5

emission in the green region (511–600 nm) which however appears in the higher wavelength region. Further, O_i and O_{Zn} in 650–750 nm correspond to the orange-red region [32].

In the doped ZnO, the increase in number of oxygen vacancies, interstitial oxygen, Zn vacancies, Zn interstitials results in the enhancement of the magnetism and electrical properties of the material.

3.7. Magnetic properties

Magnetization characteristics of the synthesized $Zn_{1-x}Ni_xO$ NPs (for x = 0.00, 0.05, 0.15, 0.20) in the ±18 kOe range measured at room temperature are shown in Fig. 7. The *M-H* curves of the pure ZnO and Ni-doped ZnO nanoparticles, with up to 15 at.%, exhibited diamagnetic behaviour at a high magnetic field and weak ferromagnetic (FM) behaviour in the lowest field regime. Sundarsan *et al.* [33] and Guruvammal *et al.* [34] reported that the pure ZnO nanoparticles exhibited ferromagnetic nature at room temperature due to the exchange interaction between localized electron spin moments resulting from oxygen vacancies at the surface of nanoparticles. The existence of ferromagnetism in $Zn_{1-x}Ni_xO$ may be due to the clustering of metallic nickel for which intrinsic ferromagnetism rises from the charge carriers. This could be verified from XRD results, clearly indicating the absence of clustering of metallic nickel phase in the sample, and therefore, the observed ferromagnetism at room temperature is an intrinsic property of Ni-doped ZnO.

Purely diamagnetic behaviour of the pure ZnO and doped sample with up to 15 at.% Ni at low applied magnetic field is due to the presence of oxygen vacancies which is confirmed by PL studies. Diamagnetic properties can also be attributed to the lattice distortion as well as size effect. Further increased Ni doping concentration leads to the enhancement of more uncompensated surface spins when compared to the bulk sample which results in an increased magnetization. However, the lowest doping of 5 at.% and higher doping 20 at.% of Ni doped ZnO nanoparticles have shown relatively weak ferromagnetic behaviour to strong trace of ferromagnetism with clear hysteresis loops. Increased magnetization is due to the decreasing particle size or crystallite size due to the nickel clustering. Literature suggests that the nickel doped ZnO have ferromagnetic nature due to the secondary phases as shown by Zhou *et al.* [35], Sharma *et al.* [36] and Xu *et al.* [37]. For the investigated samples there are no secondary phases up to 15 at.% of nickel doping except for a small trace of NiO in the sample with 20 at.% of Ni. Ferromagnetic property of the nickel doped ZnO sample therefore, can be attributed to oxygen vacancies, size effect and exchange interaction between doped transition metal ion and oxygen ion spins.

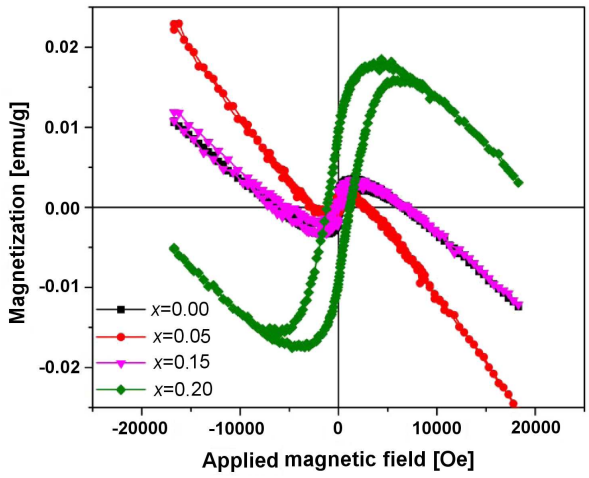

Figure 7. *M-H* loops of $Zn_{1-x}Ni_xO$ samples

An appropriate explanation for the observed room temperature ferromagnetic behaviour [38,39] (RTFM) in our nickel doped samples is the ferromagnetic exchange mechanism involving oxygen vacancies model. This is explained in terms of two reasons:

- Due to the number of oxygen vacancies (V_O) and zinc interstitials (V_{Zn}).
- Due to the exchange interaction between doped transition metal ion and O ion spins.

In the investigated samples, weak ferromagnetism arises due to the intrinsic factor which is highly correlated with the structural defects [40,41]. During annealing process, the structural defects such as V_{Zn} and V_O would likely be generated as observed in PL studies and these defects can overlap with the dopant ions such as nickel as well as adjacent defects which induces a ferromagnetic coupling between dopant spins. Thus, the magnetic coupling between Ni ions with ZnO is FM mediated by V_{Zn} and V_O and this may account for the observed RTFM and indicates that defects play a role to get a FM coupling. Further, in the present case, for low magnetic field, the ferromagnetic behaviour can be attributed to the presence of small magnetic dipoles located at the surface of nanocrystals, which interact with their nearest neighbours inside the crystal involving oxygen vacancies.

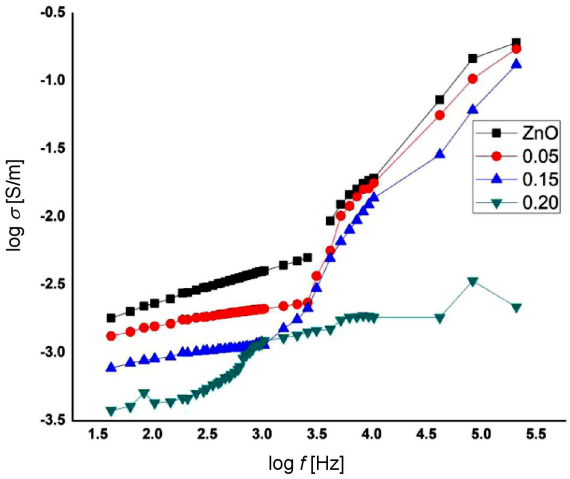

Figure 8. Conductivity variation with log of frequency for $Zn_{1-x}Ni_xO$

3.8. Electrical properties

Figure 8 shows the analysis of conductivity variation with frequency which supports the correlated barrier hopping (CBH) model for different compositions analysed in a temperature range 290–370 K. Conductivity increases with the increase in frequency for all compositions as the charge carrier jumps over a potential barrier between the defect states as observed by Mhamdi *et al.* [42]. Total conductivity of the system is given by:

$$\sigma = \sigma_{DC}(T) + \sigma_{AC}(\omega, T) \tag{4}$$

First term in the above equation is DC conductivity $\sigma_{DC}(T)$, and it is independent of frequency. The power law that governs this property for many amorphous semiconductors and insulators is given by:

$$\sigma_{AC} = \sigma_{AC}(\omega, T) = A \cdot \omega^s \tag{5}$$

where ω is angular frequency, A is a constant and s is a frequency exponent, generally less than or equal to 1. Since the DC conductivity represents the AC conductivity in the limit $\omega \to 0$, Eq. 4 cannot be used. Therefore σ_{AC} was calculated using the relation [43]:

$$\sigma_{AC} = \varepsilon_0 \cdot \varepsilon' \cdot \tan\delta \tag{6}$$

where ε_0 is the permittivity of free space, ε' dielectric constant and $\tan\delta$ is the imaginary permittivity.

AC conductivity, σ_{AC}, increases within the measured temperature range and frequency range (12 Hz–200 kHz). The AC conductivity is nearly constant at low frequencies as seen in Fig. 8, and above a certain characteristic frequency called the critical frequency, it increases according to the power law. At low frequencies, charge carriers are drifted over large distances by the applied electric forces to retain almost constant values is recorded. Ultimately, when frequency is raised, the mean displacement of the charge carriers is reduced. After reaching the critical frequency ω_p, the real part of conductivity follows the law $\sigma_{AC} \sim \omega^s$ with $0 \le s \le 1$ characterizing hopping conduction. Thus, the term $A \cdot \omega^s$ in Eq. 5 can often be elucidated on the basis of two distinct mechanisms for carrier conduction [44,45]: i) quantum mechanical tunnelling (QMT) through the barrier separating the localized sites near the Fermi level, ii) correlated barrier hopping (CBH) over the same barrier that is defined as a sudden displacement of a charge carrier from one to another neighbouring position and generally includes both jumps over a potential barrier separating them rather than tunnelling through the barrier. Further, at particularly high temperatures the orientation polarization is the dominant mechanism while at low frequencies, the hopping electrons are trapped by structural inhomogeneities existing in the crystal structure.

This behaviour with the increase in conductivity is quite acceptable in all doped ZnO samples due to the presence of Ni-dopant which increases the number of oxygen vacancies and Zn interstitials in the crystal, which in turn leads to an increase in the dipole moment adding to the effect of CBH. This results in the improved conductivity at high frequencies in Ni-doped ZnO, while in the case of the undoped ZnO hopping is hindered due to the lack of oxygen vacancies leading to a decrease in dipole moment and accordingly results in non-variance of power law.

3.9. Dielectric properties

Dielectric constant as a function of frequency for all compositions measured is shown in Fig. 9. It can be seen that the dielectric constant decreases with the increase in frequency and becomes almost constant at high frequencies for all samples. The observed high value of the dielectric constant at low frequencies and high temperatures is due to the very high contact capacitance (C_c) at electrode ($\varepsilon_r = \varepsilon/\varepsilon_0$). The capacitance associated with this layer is inversely proportional to width of the depletion layer [46]. The dielectric constant at low frequencies decreases with the applied voltage, confirming that

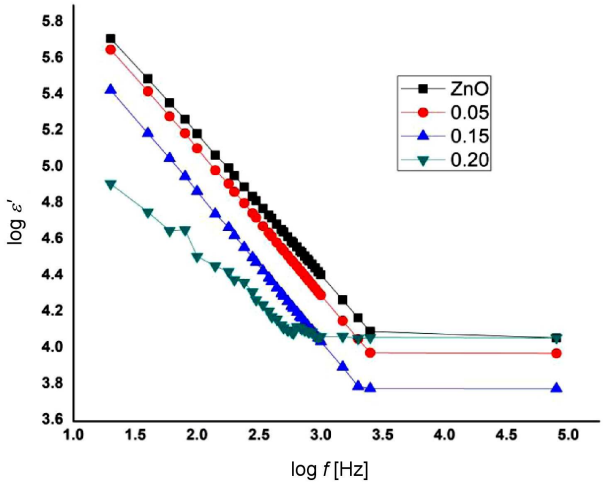

Figure 9. Variation of real part permittivity (ε') with log f

the effect at low frequency is due to the electrode polarization.

Dielectric medium composes of well conducting grains separated by poorly conducting (or resistive) grain boundaries. The charge carriers can easily migrate through the grains under the applied external electric field, but are accumulated at the grain boundaries, producing large polarization and high dielectric constant. On the basis of interfacial/space charge polarization the higher value of dielectric constant can be explained due to the inhomogeneous dielectric structure.

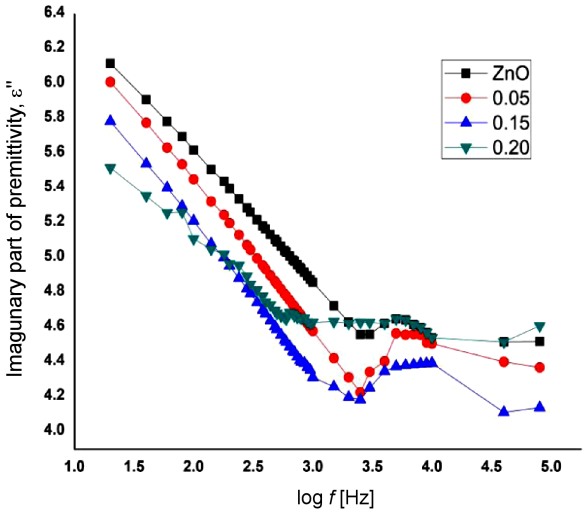

Figure 10. Variation of imaginary part of permittivity (ε'') with log f

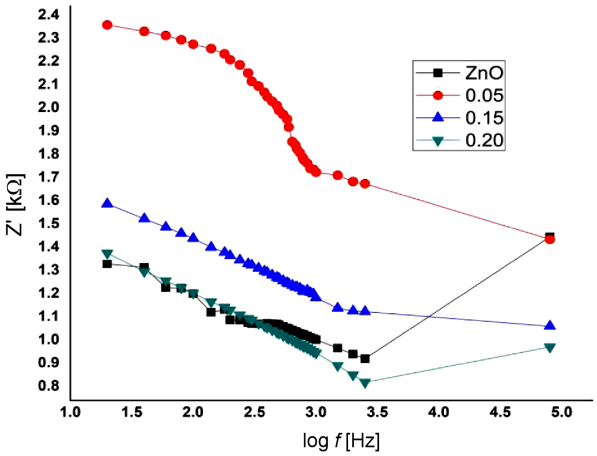

Figure 11. Variation of real part (Z') with log f

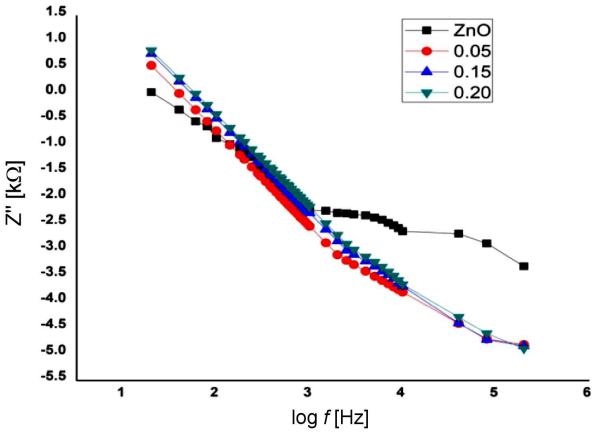

Figure 12. Variation of imaginary part (Z'') with log f

Beyond a certain frequency of external field, the hopping between different metal ions (Zn^{4+}, Zn^{2+}, Ni^{3+}, Ni^{4+}) cannot follow the alternating field, thus the polarization decreases with increase in frequency and then reaches a constant value. Imaginary part of permittivity decreases with increase in nickel concentration at lower frequency, which can be observed in Fig. 10. This is due to the small dielectric polarizability nature of nickel ions (1.23 Å^3) when compared to ZnO (2.09 Å^3). Hence, as the dopant concentration increases more zinc ions will be substituted by the nickel ions and thereby decrease the dielectric polarization, which in turn decreases the dielectric constant. Decreasing polarization also results in reduction of loss which can be measured through loss tangent.

Figure 11 shows the variation of the real part of impedance (Z') as a function of frequency. It has been observed that Z' decreases with the increase in frequency for all the compositions. This is due to the increase in conductivity with frequency resulting from hopping phenomenon. It can also be seen from Fig. 11 that Z' has strong frequency dependence in the lower frequency region and shows frequency independent behaviour in the higher frequency region. This can be attributed to the fact that low frequency region corresponds to high resistivity due to the effectiveness of resistive grain boundaries in this region. Moreover, Z' increases with the increase in doping. It is due to the increase in barrier height with doping. Figure 12 shows the variation of reactive part of impedance (Z'') as a function of frequency and composition with a similar behaviour as Z'. Reactive part of impedance (Z'') increases with the increase in dopant concentration, due to the decrease in capacitance nature at the grain boundary. It is well known that Z'' is inversely proportional to capacitance. When the capacitive and resistive components of the impedance data of material is plotted in a complex plane plot it appears in the form of sequence of semicircles representing electrical phenomenon due to the bulk (grain) material, grain boundary and interfacial phenomenon.

Generally, in high frequency region, the grains are effective while the grain boundaries are effective in low frequency region. Semicircle shows grain contributions in the high frequency region due to the bulk and grain boundary conduction while in the low frequency region, they correspond to the grain boundary contribution representing bulk properties of the material [47]. The electrical characteristic of a material is exhibited by the appearance of semicircular arcs in Nyquist plots. Figure 13 shows the complex impedance plots (Nyquist plots)

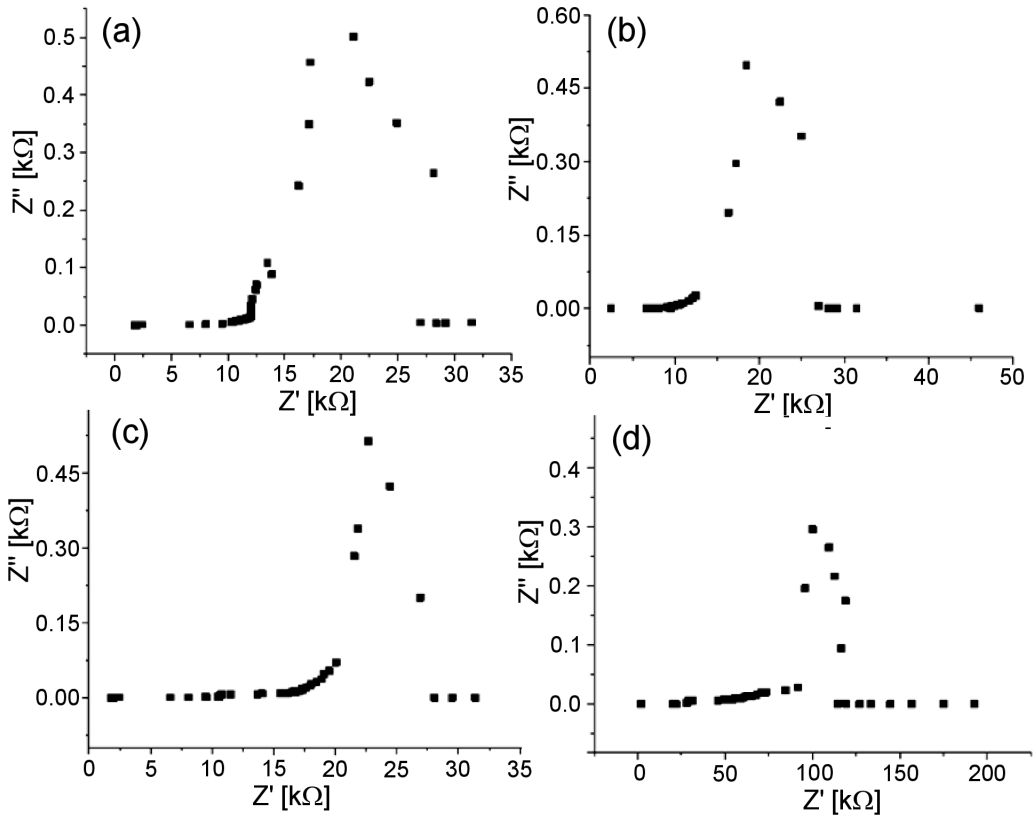

Figure 13. Cole-Cole or Nyquist plots for different compositions at room temperature for of pure ZnO (a) and Ni-doped $Zn_{1-x}Ni_xO$ nanoparticles with: b) 5, c) 15 and d) 20 at.% Ni

of pure and Ni-doped ZnO nanoparticles and similar behaviour is given by Cherifi *et al.* [44] and Omri *et al.* [48]. It has been reported in literature that the resistivity of a polycrystalline material, in general, increases with the decrease in grain size.

IV. Conclusions

Pure and Ni-doped ZnO ($Zn_{1-x}Ni_xO$, x = 0.05, 0.10, 0.15, 0.20) nanoparticles with hexagonal wurtzite structure were synthesized. The samples with up to 15 at.% of Ni are without any secondary phases, while the presence of NiO in the sample with 20 at.% of Ni was observed. SEM images reveal smaller grain size and spherical shape of Ni-doped samples while TEM confirms the particle size ~20 nm. Spectroscopic investigation using FTIR analysis shows the nickel incorporation in the wurtzite structure and changes observed at different vibrational modes. Room temperature weak ferromagnetic behaviour for the nickel doped ZnO samples was attributed to the exchange interaction between doped transition metal (Ni) ion and oxygen ion spins and presence of these defects are confirmed by PL studies. Electrical conductivity elucidates the semiconductor behaviour of these materials with conductivity which increases significantly with the increase in nickel doping in ZnO. Explanation for this behaviour is due to the correlated barrier hopping (CBH) model for different compositions at temperature 290–370 K. Complex impedance spectra demonstrate the existence of semicircle suggesting the dominance of grain boundary resistance in the nickel doped samples.

References

1. G.F. Wang, Q. Peng, Y.D. Li, "Lanthanide-doped nanocrystals: Synthesis, optical-magnetic properties, and applications", *Acc. Chem. Res.*, **44** (2011) 322–332.
2. F. Pan, C. Song, X.J. Liu, Y.C. Yang, F. Zeng, "Ferromagnetism and possible application in spintronics of transition-metal-doped ZnO films", *Mater. Sci. Eng.*, **62** (2008) 1–35.
3. Y.M. Cho, W.K. Choo, H. Kim, D. Kim, Y. Ihm, "Effects of rapid thermal annealing on the ferromagnetic properties of sputtered $Zn_{1-x}(Co_{0.5}Fe_{0.5})_xO$ thin films", *Appl. Phys. Lett.*, **80** (2002) 3358–3360.
4. H. Saeki, H. Tabata, T. Kawai, "Magnetic and electric properties of vanadium doped ZnO films", *Solid State Commun.*, **120** (2001) 439–444.
5. H. Guo, J. Zhou, Z. Lin, "ZnO nanorod light-emitting diodes fabricated by electrochemical approaches", *Electrochem. Commun.*, **10** (2008) 146–150.
6. K.N. Hui , K.S. Hui, Q. Xia, T.V. Cuong, Y.-R. Cho, J. Singh, P. Kumar, E.J. Kim, "Enhanced light extraction efficiency of GaN-based LED with ZnO nanorod grown on Ga-doped ZnO seed layer", *ECS Solid State Lett.*, **2** (2013) 43–46.
7. X. Fang, J. Li, D. Zhao, D. Shen, B. Li, X. Wang, "Phosphorus-doped p-type ZnO nanorods and ZnO nanorod p-n homojunction LED fabricated by hydrother-

mal method", *J. Phys. Chem. C*, **113** (2009) 21208–21212.
8. A. Becheri, M. Durr, L.P. Nostro, P. Baglioni, "Synthesis and characterization of zinc oxide nanoparticles: application to textiles as UV-absorbers", *J. Nanoparticle Res.*, **10** (2008) 679–689.
9. D. Liu, T.L. Kelly, "Perovskite solar cells with a planar heterojunction structure prepared using room-temperature solution processing techniques", *Nature Photonics*, **8** (2013) 133–138.
10. H. Zhou, Y. Zhang, C.-K. Mai, S.D. Collins, G.C. Bazan, T.-Q. Nguyen, A.J. Heeger, "Polymer homo-tandem solar cells with best efficiency of 11.3%", *Adv. Mater.*, **27** (2015) 1767–1773.
11. V. Vohra, K. Kawashima, T. Kakara, T. Koganezawa, I. Osaka, K. Takimiya, H. Murata, "Efficient inverted polymer solar cells employing favourable molecular orientation", *Nature Photonics*, **9** (2015) 403–408.
12. X.M. Zhang, M.Y. Lu, Y. Zhang, I.J. Chen, Z.L. Wang, "Fabrication of a high-brightness blue-light-emitting diode using a ZnO-nanowire array grown on p-GaN thin film", *Adv. Mater.*, **21** (2009) 2767–2770.
13. K. Radzimska, A. Jesionowski, "Zinc oxide - from synthesis to application: A review", *Materials*, **7** (2014) 2833–2881.
14. S.Y. Lee, E.S. Shim, H.S. Kang, S.S. Pang, J.S. Kang, "Fabrication of ZnO thin film diode using laser annealing", *Thin Solid Films*, **473** (2005) 31–34.
15. D.S. Bohle, C.J. Spina, "Controlled Co(II) doping of zinc oxide nanocrystals", *J. Phys. Chem. C*, **114** (2010) 18139–18145.
16. C.G. Jin, Y. Gao, X.M. Wu, M.L. Cui, L.J. Zhuge, Z.C. Chen, B. Hong, "Structural and magnetic properties of transition metal doped ZnO films", *Thin Solid Films*, **518** (2010) 2152–2156.
17. T. Dietl, H. Ohno, "Engineering magnetism in semiconductors", *Mater. Today*, **9** (2006) 18–26.
18. C. Liu, F. Yun, H. Morkoc, "Ferromagnetism of ZnO and GaN: A review", *J. Mater. Sci.*, **16** (2005) 555–595.
19. T. Fukumura, H. Toyosaki, Y. Yamada "Magnetic oxide semiconductors", *Semicond. Sci. Technol.*, **20** (2005) 103–111.
20. P.V. Radovanovic , D.R. Gamelin, "High-temperature ferromagnetism in Ni^{2+}-doped ZnO aggregates prepared from colloidal diluted magnetic semiconductor quantum dots", *Phys. Rev. Lett.*, **91** (2003) 157202.
21. B.U. Haq, R. Ahmed, G. Abdellatif, A. Shaari, F.K. Butt, M.B. Kanoun, S. Goumri-said, "Dominant ferromagnetic coupling over antiferromagnetic in Ni doped ZnO: First-principles calculations", *Front. Phys.*, **11** [1] (2016) 117101.
22. D.A. Schwartz, K.R. Kittilstved, D.R. Gamelin, "Above-room-temperature ferromagnetic Ni^{2+}-doped ZnO thin films prepared from colloidal diluted magnetic semiconductor quantum dots", *Appl. Phys. Lett.*, **85** (2004) 1395–1397.
23. B. Pal, D. Sarkar, P.K. Giri, "Structural, optical, and magnetic properties of Ni doped ZnO nanoparticles: Correlation of magnetic moment with defect density", *Appl. Surface Sci.*, **356** (2015) 804–811.
24. Y. Liu, H. Liu, Z. Chen, N. Kadasala, C. Mao, Y. Wang, Y. Zhang, H. Liu, Y. Liu, J. Yang, Y. Yan, "Effects of Ni concentration on structural, magnetic and optical properties of Ni-doped ZnO nanoparticles", *J. Alloys Compd.*, **604** (2014) 281–285.
25. S. Tüzemen, S. Doğan, A. Ateş, M. Yıldırım, G. Xiong, J. Wilkinson, R.T. Williams, "Convertibility of conductivity type in reactively sputtered ZnO thin films", *Phys. Status Solidi*, **195** (2003) 165–170.
26. B. Pal, S. Dhara, P.K. Giri, D. Sarkar, "Evolution of room temperature ferromagnetism with increasing 1D growth in Ni-doped ZnO nanostructures", *J. Alloys Compd.*, **647** (2015) 558–565.
27. G. Srinet, R. Kumar, V. Sajal, "Structural, optical, vibrational, and magnetic properties of sol-gel derived Ni doped ZnO nanoparticles", *J. Appl. Phys.*, **114** (2013) 033912.
28. V. Gandhi, R. Ganesan, H.H. Abdulrahman Syedahamed, M. Thaiyan, "Effect of cobalt doping on structural, optical, and magnetic properties of ZnO nanoparticles synthesized by coprecipitation method", *J. Phys. Chem. C*, **118** (2014) 9715–9725.
29. G. Vijayaprasath, R. Murugan, S. Asaithambi, G. Anandha Babu, P. Sakthivel, T. Mahalingam, Y. Hayakawa, G. Ravi, "Structural characterization and magnetic properties of Co co-doped Ni/ZnO nanoparticles", *Appl. Phys. A*, **122** (2016) 122.
30. K. Kumar, B. Nandan, P. Formanek, M. Stamm, "Fabrication of carbon microtubes from thin films of supramolecular assemblies via self-rolling approach", *J. Mater. Chem.*, **21** (2011) 10813–10817.
31. G.H. Mhlongo, K. Shingange, Z.P. Tshabalala, B.P. Dhonge, F.A. Mahmoud, B.W. Mwakikunga, D.E. Motaung, "Room temperature ferromagnetism and gas sensing in ZnO nanostructures: Influence of intrinsic defects and Mn, Co, Cu doping", *Appl. Surf. Sci.*, **390** (2016) 804–815.
32. D. Gao, Z. Zhang, J. Fu, Y. Xu, J. Qi, D. Xue. "Room temperature ferromagnetism of pure ZnO nanoparticles", *J. Appl. Phys.*, **105** (2009) 113928–113932.
33. A. Sundaresan, R. Bhargavi, N. Rangarajan, U. Siddesh, C.N.R. Rao, "Ferromagnetism as a universal feature of nanoparticles of the otherwise nonmagnetic oxides", *Phys. Rev. B*, **74** (2006) 161306.
34. D. Guruvammal, S. Selvaraj, S. Meenakshi Sundar, "Effect of Ni-doping on the structural, optical and magnetic properties of ZnO nanoparticles by solvothermal method", *J. Alloys Compd.*, **682** (2016) 850–855.
35. S. Zhou, K. Potzger, H. Reuther, K. Kuepper, W. Skorupa, M. Helm, J. Fassbender, "Absence of ferromagnetism in V-implanted ZnO single crystals", *J. Appl. Phys.*, **101** (2007) 9.
36. P.K. Sharma, R.K. Dutta, R.J. Choudhary, A.C. Pandeys, "Doping, strain, defects and magneto-optical properties of $Zn_{1-x}Mn_xO$ nanocrystals", *Cryst. Eng. Com.*, **15** (2013) 4438–4447.
37. K. Xu, C. Liu, R. Chen, X. Fang, X. Wu, J. Liu, "Structural and room temperature ferromagnetic properties of Ni doped ZnO nanoparticles via low-temperature hydrothermal method", *Physica B: Condensed Matter*, **502** (2016) 155–159.
38. V. Pazhanivelu , A. Paul Blessington Selvadurai , R. Kannan, R. Murugaraj, "Room temperature ferromagnetism in I^{st} group elements codoped ZnO: Fe nanoparticles by coprecipitation method", *Physica B: Condensed Matter*, **487** (2016) 102–108.
39. J.M.D. Coey, M. Venkatesan, C.B. Fitzgerald, "Donor impurity band exchange in dilute ferromagnetic oxides", *Nat.*

Mater., **4** (2005) 173–179.
40. B. Khalil, H. Labrim, O. Mounkachi, B. Belhorma, A. Benyoussef, A. El Kenz, E. Ntsoenzok, "Origin of magnetism from native point defects in ZnO", *J. Supercond. Nov. Magn.*, **25** (2012) 1145–1150.
41. M. Naeem, S.K. Hasanain, M. Kobayashi, Y. Ishida, A. Fujimori,S. Buzby, S.I. Shah, "Effect of reducing atmosphere on the magnetism of $Zn_{(1-x)}Co_{(x)}O$ ($0 \leq x \leq 0.10$) nanoparticles", *Nanotechnol.*, **17** (2006) 2675–2680.
42. A. Mhamdi, B. Ouni, A. Amlouk, K. Boubaker, M. Amlouk, "Study of nickel doping effects on structural, electrical and optical properties of sprayed ZnO semiconductor layers", *J. Alloys Compd.*, **582** (2014) 810–822.
43. S. Kurien, J. Mathew, S. Sebastian, S.N. Potty, K.C. George, "Dielectric behavior and ac electrical conductivity of nanocrystalline nickel aluminate", *Mater. Chem. Phys.*, **98** (2006) 470–476.
44. Y. Cherifi, A. Chaouchi, Y. Lorgoilloux, Md. Rguiti, A. Kadri, C. Courtois, "Electrical, dielectric and photocatalytic properties of Fe-doped ZnO nanomaterials synthesized by sol gel method", *Process. Appl. Ceram.*, **10** [3] (2016) 125–135.
45. A.K. Jonscher, "The 'universal' dielectric response", *Nature*, **267** (1977) 673–679.
46. M. Idrees, M. Nadeem, M. Atif, M. Siddique, M. Mehmood, M. Hassan, "Origin of colossal dielectric response in $LaFeO_3$", *Acta Mater.*, **59** [4] (2011) 1338–1345.
47. A. Yildiz, B. Kayhan , B. Yurduguzel, A.P. Rambu, F. Iacomi , S. Simon, "Electrical conduction properties of Co-doped ZnO nanocrystalline thin films", *J. Mater. Sci.: Mater. Electron.*, **23** (2012) 425–430.
48. K. Omri, I. Najeh, L. El Mir, "Influence of annealing temperature on the microstructure and dielectric properties of ZnO nanoparticles", *Ceram. Int.*, **42** (2016) 8940–8948.